mathematics

MDPI

Article

Dynamic Condensation-Based Reduction Method for Precise Broadband Frequency Analysis

Geomji Choi [1], Juhwan Lee [2,*] and Seongmin Chang [1,*]

[1] School of Mechanical Engineering, Chungnam National University, Daejeon 34134, Republic of Korea; gchoi@o.cnu.ac.kr
[2] Genesis Electrified Propulsion NVH Test Team, Hyundai Motor Group, Seoul 06797, Republic of Korea
* Correspondence: juhwan1109@hyundai.com (J.L.); schang@cnu.ac.kr (S.C.)

Abstract: In this paper, we propose a degree-of-freedom-based adaptive reduction method that ensures accuracy over a wide band. In the conventional dynamic condensation method, a single reduced model consisting of low-order modes is used throughout the analysis. This results in low accuracy in the high-frequency band because it does not reflect the characteristics of the frequencies. To address this issue, we implemented a reduced model for each frequency using a Taylor series. This method converts the transformation matrix into a frequency-independent form, which allows for a simple interpolation of the reduction model by updating the differences between frequencies. Numerical examples were adopted to examine the accuracy and efficiency of the proposed method.

Keywords: reduced order modeling; dynamic reduction method frequency analysis

MSC: 70-08

1. Introduction

With the advancements in computer resources, the utilization of computational analysis has increased in the fields of structures and vibrations. In the past, analysis was used for a conservative design to verify whether a structure would fracture. Currently, it is widely used for problems that require high accuracy, such as prognostics and health management, and predicting the behavior of physical systems using digital twins. These techniques may require precise physics-based models to obtain computational responses that are very similar to the experimental data. To implement these models, the same analytical process needs to be repeated by changing some design variables. Furthermore, while previous research focused on the low-mode behavior of the structures, there has recently been a growing interest in their behavior in the mid- to high-frequency range. For example, in the developing electric vehicle industry, the importance of analyzing electromagnetic vibrations and high-frequency noise, which were not previously considered issues, is increasing [1–4]. However, as the frequency increases, the structure exhibits different behaviors in specific parts, such as near its natural frequencies, unlike in the low-frequency range. To analyze these ranges accurately, it is necessary to perform a dynamic analysis for each frequency, which requires a repeated process. These examples imply that iterative analyses, which have recently been in demand, may be inefficient because they require the recalculation of operations that remain unchanged in the structural composition. In addition, as the demand for analyzing assembled structures increases, considerable calculation time is required. Therefore, computational techniques that can efficiently perform repeated analyses of large structures are required.

check for updates

Academic Editor: Patricia J. Y. Wong

Received: 28 November 2024
Revised: 23 December 2024
Accepted: 27 December 2024
Published: 28 December 2024

Citation: Choi, G.; Lee, J.; Chang, S. Dynamic Condensation-Based Reduction Method for Precise Broadband Frequency Analysis. *Mathematics* **2025**, *13*, 81. https://doi.org/10.3390/math13010081

Copyright: © 2024 by the authors. Licensee MDPI, Basel, Switzerland. This article is an open access article distributed under the terms and conditions of the Creative Commons Attribution (CC BY) license (https://creativecommons.org/licenses/by/4.0/).

One method to solve this problem is to use a reduced order model (ROM). The ROM is created using a reduced basis (RB) that extracts the main features of the full order model (FOM). Because the characteristics of the RB have a significant influence on the ROM, various studies have been conducted on how to construct it [5–12]. One of them is the condensation method, which constructs a ROM based on the relationship between the degrees of freedom (DOF) in the physical coordinates of the system. In this method, the total DOF are divided into master and slave DOF, and the FOM is converted into a ROM of the size of the master DOF using a transformation matrix, which is the relationship between the two DOF. This method was first proposed in 1965 by Guyan [13] for static systems that ignored the inertial forces. Based on this approach, analytical methods suitable for dynamic systems that consider inertial forces have been devised [14–21]. A characteristic of these methods is that a single ROM composed of low-order modes is used throughout the analysis. The previously proposed RB for dynamic systems has a form that depends on the unknown frequency. Although it differs in some details, it is usually replaced by a frequency-independent form through the Maclaurin series. This implies that it is mathematically assumed based on a reference frequency of 0. This assumption leads to accurate results in the low-frequency band owing to the convergence radius for the reference, but it has a limitation in that the accuracy decreases in the high-frequency band outside the radius. This is a challenge that needs to be overcome, considering the wide frequency of interest in recent analyses.

In this paper, we propose a DOF-based reduction method that can implement accurately reduced models, even at broadband frequencies. The proposed method efficiently generated reduced models at all frequencies using a Taylor series. Unlike the Maclaurin series, the Taylor series expresses the transformation matrices as polynomials based on the power difference between the reference and variable frequencies. This formula allows simple interpolation by reusing the transformation matrix calculated at the reference point and updating the interval of the transformation matrix at the variable point. In addition, because the reference point is not limited to one point, when the formula is expanded at a shift point, accurate interpolation is possible even at high frequencies by overcoming the limitations of the convergence radius. Moreover, by presenting an appropriate convergence range through a geometrical method that uses the order difference in the transformation matrix, the problem of decreased accuracy owing to the radius can be partially solved.

This paper is organized as follows: In Section 2, the formulation of the dynamic equation and existing reduction methods are reviewed, and the details of the proposed method are presented. Section 3 verifies the efficiency and accuracy of the proposed method using several numerical examples. A summary and the conclusions are presented in Section 4.

2. Mathematical Formulation

In this section, we describe the process of converting a general time-based dynamic equation into a frequency-based equation. After representing the model order reduction, the processes and limitations of previous methods were reviewed. Finally, we describe the construction of the proposed method and its limitations.

2.1. Formulation of Dynamic Analysis for Harmonic Response

Dynamic equations typically describe the time-varying system states. Based on Newton's second law, the motion of the equations can be expressed as the summation of the inertial, damping, and restoring forces as follows:

$$\widetilde{\mathbf{M}}\frac{d^2\mathbf{u}(t)}{dt^2} + \widetilde{\mathbf{C}}\frac{d\mathbf{u}(t)}{dt} + \widetilde{\mathbf{K}}\mathbf{u}(t) = \mathbf{f}(t), \tag{1}$$

where $\widetilde{\mathbf{M}}$, $\widetilde{\mathbf{C}}$, and $\widetilde{\mathbf{K}}$ are the mass, damping, and stiffness matrices, respectively. **u** and **f** are the displacement and force vectors, respectively. When N is the size of the total DOF, the matrix and vector sizes are $N \times N$ and $N \times 1$, respectively.

The Newmark method [22] is typically used to solve differential equations over time. The method sets the initial position, velocity, and acceleration of the system and calculates the acceleration of the $(n+1)-th$ time step using the $n-th$ time step. The velocity and displacement of the $(n+1)-th$ time step are updated based on the calculated acceleration. This method can directly obtain a solution to the equation. However, the state of the system must be tracked at each time step, which is time-consuming.

In structural systems, the external forces are often equivalent to harmonic forces. Frequency-based equations were obtained by assuming a response to harmonic solutions. The second-order differential equation was changed to a quadratic equation, and the computational process for obtaining the solution was simplified. Most systems respond differently, depending on the input frequency. This converted equation allowed us to clearly understand the response of the target system to the external forces. Most importantly, the number of calculations is greatly reduced because the analysis can be performed in the desired frequency band. In this context, this study addresses an analysis system transformed from the time domain to the frequency domain via a Fourier transform. To understand the dynamic characteristics of the system more clearly, the solution is assumed to be a complex harmonic response. The force and displacement vectors in Equation (1) are expressed as follows:

$$\mathbf{f}(t) = \mathbf{F}_0(cos(wt+\phi) + isin(wt+\phi)) = \mathbf{F}_0 e^{i(wt+\phi)}, \tag{2}$$

$$\mathbf{u}(t) = \mathbf{X}_0(cos(wt+\phi) + isin(wt+\phi)) = \mathbf{X}_0 e^{i(wt+\phi)}, \tag{3}$$

where $\mathbf{F}_0$ and $\mathbf{X}_0$ denote the amplitudes of the force and displacement functions, respectively. w is the angular frequency, and ϕ is the phase difference. By substituting Equations (2) and (3) into the vector of Equation (1), a frequency-based dynamic equation is generated as follows:

$$\left(-w^2\widetilde{\mathbf{M}} + iw\widetilde{\mathbf{C}} + \widetilde{\mathbf{K}}\right)\mathbf{X}_0 e^{i(wt+\phi)} = \mathbf{F}_0 e^{i(wt+\phi)}. \tag{4}$$

In the finite element method, rigid body modes occur in systems without boundary conditions. Since the eigenvalues of the rigid body modes are 0, the matrices of the system are positive semidefinite. When the boundary conditions are imposed on the system so that the matrix satisfies positive define, Equation (4) is rewritten as follows:

$$\left(-w^2\mathbf{M} + iw\mathbf{C} + \mathbf{K}\right)\mathbf{X} e^{i(wt+\phi)} = \mathbf{F} e^{i(wt+\phi)}, \tag{5}$$

where **M**, **C**, and **K** are the mass, damping, and stiffness matrices with boundary conditions, respectively. **F** and **X** are the amplitudes of the force and displacement functions with boundary conditions, respectively. When the size of the boundary conditions is nBC, the matrix and vector sizes are $(N - nBC) \times (N - nBC)$ and $(N - nBC) \times 1$, respectively. Since the matrix $\left(-w^2\mathbf{M} + iw\mathbf{C} + \mathbf{K}\right)$ is invertible, the frequency responses are obtained as follows:

$$\mathbf{X} = \left(-w^2\mathbf{M} + iw\mathbf{C} + \mathbf{K}\right)^{-1}\mathbf{F} = {\mathbf{K}_e}^{-1}\mathbf{F}, \tag{6}$$

where $\mathbf{K}_e$ denotes the effective stiffness matrix. Because the function contains frequencies as input variables, the inverse matrix of the effective stiffness matrix must be calculated at each frequency step to obtain an accurate response. However, performing an inverse matrix operation is time-consuming. As the time required for the inverse matrix operation

is proportional to the cube of the size of the matrix, it is important to reduce the matrix size. To solve this problem, we adopted a degree-of-freedom-based ROM and intended to provide an improved ROM by reviewing existing ROMs.

2.2. Review of Existing Condensation Method

This subsection introduces two major model reduction methods for efficient system computation. When the external force is zero and the damping force is removed, Equation (5) becomes the following eigenvalue problem:

$$(\mathbf{K} - \mathbf{\Lambda M})\mathbf{X} = 0 \; where \; \mathbf{\Lambda} = w^2, \tag{7}$$

where $\mathbf{\Lambda}$ is an eigenvalue. Equation (7) can be expressed as a matrix divided into master and slave DOF as follows:

$$\begin{bmatrix} \mathbf{K}_{mm} & \mathbf{K}_{ms} \\ \mathbf{K}_{sm} & \mathbf{K}_{ss} \end{bmatrix} \begin{Bmatrix} \mathbf{X}_m \\ \mathbf{X}_s \end{Bmatrix} - \mathbf{\Lambda} \begin{bmatrix} \mathbf{M}_{mm} & \mathbf{M}_{ms} \\ \mathbf{M}_{sm} & \mathbf{M}_{ss} \end{bmatrix} \begin{Bmatrix} \mathbf{X}_m \\ \mathbf{X}_s \end{Bmatrix} = \begin{Bmatrix} 0 \\ 0 \end{Bmatrix}, \tag{8}$$

where subscripts m and s indicate the master and slave DOF, respectively. The master DOF are the DOF that remain after the system is reduced, and the slave DOF are the DOF that are removed from the system. Namely, since the size of the master DOF determines the size of the reduced system, the number of master DOF should be less than the number of slave DOF. By expanding the second row of Equation (8), the relationship between the master and the slave DOF can be obtained as follows:

$$\mathbf{X}_s = (-\mathbf{K}_{ss} + \mathbf{\Lambda M}_{ss})^{-1}(\mathbf{K}_{sm} - \mathbf{\Lambda M}_{sm})\mathbf{X}_m, \tag{9}$$

$$\mathbf{T} = \begin{bmatrix} \mathbf{I}_{mm} \\ \mathbf{t} \end{bmatrix} = \begin{bmatrix} \mathbf{I}_{mm} \\ (-\mathbf{K}_{ss} + \mathbf{\Lambda M}_{ss})^{-1}(\mathbf{K}_{sm} - \mathbf{\Lambda M}_{sm}) \end{bmatrix}, \tag{10}$$

where $\mathbf{I}_{mm}$ is an identity matrix of size $m \times m$, and $\mathbf{T}$ is a transformation matrix of size $N \times m$. The various DOF-based reduction methods depend on the assumptions of the transformation matrix. The simplest method is the Guyan reduction method, which is based on static analysis. Neglecting the mass matrix effect ($\mathbf{\Lambda} = 0$) in Equation (10),

$$\mathbf{T}_G = \begin{bmatrix} \mathbf{I}_{mm} \\ \mathbf{t}_G \end{bmatrix} = \begin{bmatrix} \mathbf{I}_{mm} \\ -\mathbf{K}_{ss}^{-1}\mathbf{K}_{sm} \end{bmatrix}, \tag{11}$$

where $\mathbf{T}_G$ is the Guyan transformation matrix obtained by the Guyan reduction method. Using this transformation matrix, Equation (6) can be reduced to

$$\mathbf{X}_G = \left(\mathbf{K}_G - w^2\mathbf{M}_G\right)^{-1}\mathbf{F}_G, \tag{12}$$

$$\mathbf{K}_G = \mathbf{T}_G^{\mathrm{T}}\mathbf{K}\mathbf{T}_G = \mathbf{K}_{mm} + \mathbf{K}_{ms}\mathbf{t}_G, \tag{13}$$

$$\mathbf{M}_G = \mathbf{T}_G^{\mathrm{T}}\mathbf{M}\mathbf{T}_G = \mathbf{M}_{mm} + \mathbf{M}_{ms}\mathbf{t}_G + \mathbf{t}_G^{\mathrm{T}}\mathbf{M}_{sm} + \mathbf{t}_G^{\mathrm{T}}\mathbf{M}_{ss}\mathbf{t}_G, \tag{14}$$

$$\mathbf{F}_G = \mathbf{T}_G^{\mathrm{T}}\mathbf{F} = \mathbf{F}_m + \mathbf{t}_G^{\mathrm{T}}\mathbf{F}_s, \tag{15}$$

where subscript G denotes the reduced matrix by the Guyan transformation matrix.

The dynamic transformation matrix can be obtained by considering the mass-matrix effect. This method transforms the inverse part of Equation (10) into a polynomial using the

Maclaurin series. The second term of the polynomial is included in the equation. Assuming that $\mathbf{\Lambda}$ is $\mathbf{M}_G^{-1}\mathbf{K}_G$,

$$\mathbf{T}_{IRS} = \begin{bmatrix} \mathbf{I}_{mm} \\ \mathbf{t}_{IRS} \end{bmatrix} = \begin{bmatrix} \mathbf{I}_{mm} \\ -\mathbf{K}_{ss}^{-1}\mathbf{K}_{sm} + \mathbf{K}_{ss}^{-1}\left(\mathbf{M}_{sm} - \mathbf{M}_{ss}\mathbf{K}_{ss}^{-1}\mathbf{K}_{sm}\right)\mathbf{M}_G^{-1}\mathbf{K}_G \end{bmatrix}, \tag{16}$$

where $\mathbf{T}_{IRS}$ is the *IRS* transformation matrix obtained using the IRS reduction method [14]. The reduced system using the IRS transformation matrix is given by expressions similar to Equations (12)–(15):

$$\mathbf{X}_{IRS} = \left(\mathbf{K}_{IRS} - w^2\mathbf{M}_{IRS}\right)^{-1}\mathbf{F}_{IRS}, \tag{17}$$

$$\mathbf{K}_{IRS} = \mathbf{T}_{IRS}^{\mathrm{T}}\mathbf{K}\mathbf{T}_{IRS} = \mathbf{K}_{mm} + \mathbf{K}_{ms}\mathbf{t}_{IRS} + \mathbf{t}_{IRS}^{\mathrm{T}}\mathbf{K}_{sm} + \mathbf{t}_{IRS}^{\mathrm{T}}\mathbf{K}_{ss}\mathbf{t}_{IRS}, \tag{18}$$

$$\mathbf{M}_{IRS} = \mathbf{T}_{IRS}^{\mathrm{T}}\mathbf{M}\mathbf{T}_{IRS} = \mathbf{M}_{mm} + \mathbf{M}_{ms}\mathbf{t}_{IRS} + \mathbf{t}_{IRS}^{\mathrm{T}}\mathbf{M}_{sm} + \mathbf{t}_{IRS}^{\mathrm{T}}\mathbf{M}_{ss}\mathbf{t}_{IRS}, \tag{19}$$

$$\mathbf{F}_{IRS} = \mathbf{T}_{IRS}^{\mathrm{T}}\mathbf{F} = \mathbf{F}_m + \mathbf{t}_{IRS}^{\mathrm{T}}\mathbf{F}_s. \tag{20}$$

2.3. Formulation of Proposed Method

2.3.1. Basic Framework of Proposed Method

A characteristic of previous methods is the construction of a reduced matrix by assuming an eigenvalue as a matrix. A single matrix reduced by the assumed matrix was created and used for the entire analysis. This allows a large number of computations for the reduced system with only one large initial operation. However, the consistent model cannot reflect the characteristics of the entire frequency environment. For this reason, it is unavoidable that accuracy deteriorates rapidly in high-frequency bands. It is also inefficient to use in systems where accuracy within a certain range is required or where the composition of the structure is changed. To address these problems, we propose an adaptive reduction method in which the composition of the reduced model changes according to frequency. In the proposed method, Equation (8) is rewritten as follows:

$$\begin{bmatrix} \mathbf{K}_{mm} & \mathbf{K}_{ms} \\ \mathbf{K}_{sm} & \mathbf{K}_{ss} \end{bmatrix} \begin{Bmatrix} \mathbf{X}_m \\ \mathbf{X}_s \end{Bmatrix} - \lambda_i \begin{bmatrix} \mathbf{M}_{mm} & \mathbf{M}_{ms} \\ \mathbf{M}_{sm} & \mathbf{M}_{ss} \end{bmatrix} \begin{Bmatrix} \mathbf{X}_m \\ \mathbf{X}_s \end{Bmatrix} = \begin{Bmatrix} 0 \\ 0 \end{Bmatrix}, \tag{21}$$

where λ_i is the input frequency, not a matrix. Therefore, the transformation matrix is expressed as a function of frequency as follows:

$$\mathbf{T}(\lambda_i) = \begin{bmatrix} \mathbf{I}_{mm} \\ \mathbf{t}(\lambda_i) \end{bmatrix} = \begin{bmatrix} \mathbf{I}_{mm} \\ (-\mathbf{K}_{ss} + \lambda_i\mathbf{M}_{ss})^{-1}(\mathbf{K}_{sm} - \lambda_i\mathbf{M}_{sm}) \end{bmatrix}. \tag{22}$$

Since the transformation matrix changes with frequency, the reduced model also changes with frequency. The reduced system using the exact transformation matrix is expressed as follows:

$$\mathbf{X}_R = \left(\mathbf{K}_R(\lambda_i) - w^2\mathbf{M}_R(\lambda_i)\right)^{-1}\mathbf{F}_R(\lambda_i), \tag{23}$$

$$\mathbf{K}_R(\lambda_i) = \mathbf{T}(\lambda_i)^{\mathrm{T}}\mathbf{K}\mathbf{T}(\lambda_i) = \mathbf{K}_{mm} + \mathbf{K}_{ms}\mathbf{t}(\lambda_i) + \mathbf{t}(\lambda_i)^{\mathrm{T}}\mathbf{K}_{sm} + \mathbf{t}(\lambda_i)^{\mathrm{T}}\mathbf{K}_{ss}\mathbf{t}(\lambda_i), \tag{24}$$

$$\mathbf{M}_R(\lambda_i) = \mathbf{T}(\lambda_i)^{\mathrm{T}}\mathbf{M}\mathbf{T}(\lambda_i) = \mathbf{M}_{mm} + \mathbf{M}_{ms}\mathbf{t}(\lambda_i) + \mathbf{t}(\lambda_i)^{\mathrm{T}}\mathbf{M}_{sm} + \mathbf{t}(\lambda_i)^{\mathrm{T}}\mathbf{M}_{ss}\mathbf{t}(\lambda_i), \tag{25}$$

$$\mathbf{F}_R(\lambda_i) = \mathbf{T}(\lambda_i)^{\mathrm{T}}\mathbf{F} = \mathbf{F}_m + \mathbf{t}(\lambda_i)^{\mathrm{T}}\mathbf{F}_s. \tag{26}$$

2.3.2. Interpolation of Transformation Matrix

The reduced model constructed with the input frequency achieves the ideal accuracy at that frequency. However, it is very unproductive to create a reduced model at every frequency step. The creation process involves an inverse matrix operation of the size of the slave DOF in the transformation matrix calculation. Since the size of the slave DOF is similar to the size of the total DOF, as few reduced models as possible should be computed to increase the computational efficiency. This possibility has been observed in the Taylor series. This method accurately approximates the adjacent range at a single point by expressing a given function as a polynomial. Namely, when a high frequency is adopted as the point, the accuracy of the area can be improved. The Taylor expansion of a smooth function is expressed as a power series, as follows:

$$f(x) = f(c) + (x-c)f^{(1)}(c) + \frac{(x-c)^2 f^{(2)}(c)}{2!} + \cdots = \sum_{n=0}^{\infty} \frac{(x-c)^n f^{(n)}(c)}{n!}, \quad (27)$$

where c is the center point of the expansion, and x is an input variable. Equation (27) is expressed as an infinite summation of terms consisting of the function derivatives at the point. The key point to note in this equation is that the derivative is calculated only at the center point, and the variable represents the distance from the reference point. Consequently, if the value of the derivative function is stored, the function of the next variable can be predicted using the difference between the variable and reference point without calculating additional derivatives. Let $f(x)$ be expressed as $\mathbf{t}(\lambda)$, a function of the transformation matrix with respect to the scalar input variable λ. The basic form of the transformation matrix expressed in the second row of Equation (22) is expanded into a Taylor series about the centered point λ_0 as follows:

$$f(c) \rightarrow \mathbf{t}_1(\lambda_0) = -(\mathbf{K}_{ss} - \lambda_0 \mathbf{M}_{ss})^{-1}(\mathbf{K}_{sm} - \lambda_0 \mathbf{M}_{sm}), \quad (28)$$

$$(x-c)f^{(1)}(c) \rightarrow \mathbf{t}_2(\lambda_0) = (\lambda - \lambda_0)(\mathbf{K}_{ss} - \lambda_0 \mathbf{M}_{ss})^{-1}(\mathbf{M}_{ss}\mathbf{t}_1(\lambda_0) + \mathbf{M}_{sm}), \quad (29)$$

$$\frac{(x-c)^2 f^{(2)}(c)}{2!} \rightarrow \mathbf{t}_3(\lambda_0) = (\lambda - \lambda_0)^2(\mathbf{K}_{ss} - \lambda_0 \mathbf{M}_{ss})^{-1}\mathbf{M}_{ss}\mathbf{t}_2(\lambda_0), \quad (30)$$

$$\frac{(x-c)^3 f^{(3)}(c)}{3!} \rightarrow \mathbf{t}_4(\lambda_0) = (\lambda - \lambda_0)^3(\mathbf{K}_{ss} - \lambda_0 \mathbf{M}_{ss})^{-1}\mathbf{M}_{ss}\mathbf{t}_3(\lambda_0). \quad (31)$$

When examining the approximation of the transformation matrix, the heavy operation is conducted only at the point λ_0. This implies that transformation matrices of λ can be interpolated simply by multiplying the pre-generated matrix by a scalar. From Equation (30) onwards, the same mathematical rules were applied to determine the subsequent terms. When the distance between $i{-}th$ λ and the reference point is $\Delta\lambda_i$, a generalized formula for the entire transformation matrix can be derived as follows:

$$\lambda_i = \lambda_0 + \Delta\lambda_i, \quad (32)$$

$$\mathbf{t}(\lambda_i) = \mathbf{t}_1(\lambda_0) + \Delta\lambda_i \mathbf{t}_2(\lambda_0) + \sum_{n=3}^{\infty} {\Delta\lambda_i}^{n-1}(\mathbf{K}_{ss} - \lambda_0 \mathbf{M}_{ss})^{-1}\mathbf{M}_{ss}\mathbf{t}_{n-1}(\lambda_0). \quad (33)$$

Unlike Equations (22) and (33) it is calculated by reusing the transformation matrix for centered point rather than performing matrix operations for each λ_i. The corresponding transformation matrix is obtained by simple computation by updating the value of $\Delta\lambda_i$. Since the multiplication of a scalar and a matrix consumes much less time than the operation of matrices, the computational efficiency increases as the frequency range for which

interpolation is possible expands. The reduced models used in Equation (23) are rewritten as follows:

$$\mathbf{K}_R(\lambda_i) = \mathbf{K}_{mm} + \sum_{n=0}^{\infty} \Delta\lambda_i{}^n \left\{ \mathbf{K}_{ms}\mathbf{t}(\lambda_0) + \mathbf{t}(\lambda_0)^{\mathrm{T}}\mathbf{K}_{sm} + \mathbf{t}(\lambda_0)^{\mathrm{T}}\mathbf{K}_{ss}\mathbf{t}(\lambda_0) \right\}, \tag{34}$$

$$\mathbf{M}_R(\lambda_i) = \mathbf{M}_{mm} + \sum_{n=0}^{\infty} \Delta\lambda_i{}^n \left\{ \mathbf{M}_{ms}\mathbf{t}(\lambda_0) + \mathbf{t}(\lambda_0)^{\mathrm{T}}\mathbf{M}_{sm} + \mathbf{t}(\lambda_0)^{\mathrm{T}}\mathbf{M}_{ss}\mathbf{t}(\lambda_0) \right\}, \tag{35}$$

$$\mathbf{F}_R(\lambda_i) = \mathbf{F}_m + \sum_{n=0}^{\infty} \Delta\lambda_i{}^n \left\{ \mathbf{t}(\lambda_0)^{\mathrm{T}}\mathbf{F}_s \right\}. \tag{36}$$

It is important to clarify that the proposed transformation matrix is an approximate function defined at the centered point. A transformation matrix has the mathematical characteristic of multiple singular points where the determinant of the inverse matrix is zero. In other words, the matrix is no longer approximately beyond the singularity closest to the reference point. Therefore, it is important to determine the convergence radius of the center point.

2.3.3. Proof of Convergence Range with Proposed Reduction

The proposed transformation matrix is converted from the form of a rational function to the form of a geometric series with a common ratio, $\Delta\lambda_i(\mathbf{K}_{ss} - \lambda_0\mathbf{M}_{ss})^{-1}\mathbf{M}_{ss}$. We propose a method to obtain the radius of convergence geometrically through a representative example of such a transformation. The geometrical method was compared with a mathematical method to verify its validity. First, the mathematical method for determining the convergence range is explained. Let $f(x) = \frac{1}{1-x}$. The reference function can be approximated using a Taylor series expansion as follows:

$$f(x) \cong \sum_{k=1}^{n} x^{k-1} = S_n, \tag{37}$$

where S_n denotes the *n-th* partial summation of the series. Through a ratio test, the common ratio was required to satisfy the following conditions, and the convergence range R is as follows:

$$\lim_{n\to\infty} \left| \frac{S_{n+1}}{S_n} \right| < 1, \quad R : |x| < 1. \tag{38}$$

Subsequently, a geometrical method for obtaining this range is explained. To achieve this, each partial function of the series is represented graphically. Figure 1 shows the values of the function $f(x)$ and S_n for the $x \in [-2, 2]$. The approximated function S_n appeared as 15 functions, from S_1 to S_{15}, respectively.

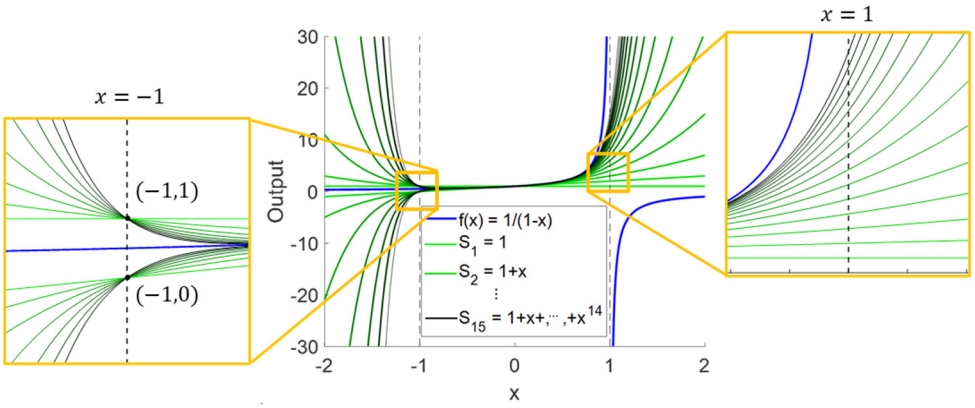


Figure 1. Comparison of reference function and *15−th* partial summation of the series.

In Figure 1, the blue line represents the rational function, and the green line represents the partial summations of the series by order. As the green color changes from light to dark, the function contains more higher-order terms. The figure shows that the higher the order of the polynomial terms, the better the approximation of a rational function within the convergence range. We focused on the tendency of each function to be expressed at the range boundaries. The values of the adjacent functions at the upper bound increase consistently. At the lower bound, the direction of divergence depends on the parity of the highest order of the polynomial, and the function value is 1 when it is even and 0 when it is odd. Differences in adjacent functions were performed to compare the values of the convergence and divergence ranges. The difference in the functions is expressed as follows:

$$V_i(x) = S_{i+1}(x) - S_i(x)\ ,\ \ where\ i = 1,\ 2,\ 3,\ \cdots,\ 14, \tag{39}$$

where $V_i(x)$ is the first-order difference, and the subscripts i and $i+1$ denote the indices of the first and second functions being different, respectively. When x is at the bounds, the absolute value of $V_i(x)$ is 1, regardless of i, indicating consistent differences between adjacent functions. Table 1 lists the absolute values of the functions for the exterior, boundary, and interior points of the convergence range. In Table 1, the distance between the physical coordinates of adjacent functions decreases as the order of the function increases within the convergence range but has the opposite pattern outside this range. Additional differences were considered to investigate the generalized characteristics of adjacent functions. The difference between the absolute values of the first-order difference is expressed as

$$W_i(x) = |V_{i+1}(x)| - |V_i(x)|\ ,\ \ where\ i = 1,\ 2,\ \cdots,\ 13, \tag{40}$$

where $W_i(x)$ denotes the second-order difference. Figure 2 depicts the values of $W_i(x)$ over the interval $[-2, 2]$. In the figure, a symmetrical shape is observed with respect to the centered point 0. In addition, the function is negative within the convergence range and positive outside the range. Therefore, the convergence radius is determined based on the change in sign, and the geometric method eventually obtains the same convergence radius as the mathematical method.

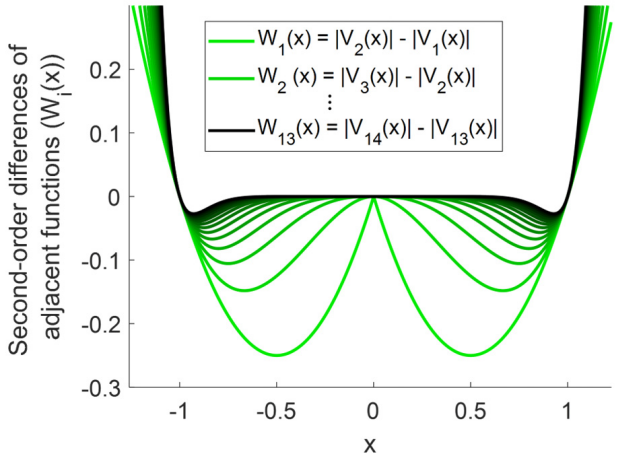


Figure 2. Comparison of the second−order differences in adjacent functions.

Table 1. Absolute values of the first-order difference at selected points.

$\lvert V_i(x)\rvert$	$x = -1.2$	$x = -1$	$x = -0.8$	$x = -0.5$	$x = 0.8$	$x = 1$	$x = 1.2$	$x = 1.7$
$\lvert V_1\rvert$	1.2	1	0.8	0.5	0.8	1	1.2	1.7
$\lvert V_2\rvert$	1.44	1	0.64	0.25	0.64	1	1.44	2.89
$\lvert V_3\rvert$	1.728	1	0.512	0.125	0.512	1	1.728	4.91
⋮	⋮	⋮	⋮	⋮	⋮	⋮	⋮	⋮
$\lvert V_{13}\rvert$	10.699	1	0.055	1.22×10^{-4}	0.055	1	10.699	990.46
$\lvert V_{14}\rvert$	12.839	1	0.044	6.10×10^{-5}	0.044	1	12.839	1.68×10^{3}

2.3.4. Implementation of Proposed Reduction

In the previous subsection, we presented two methods for determining the convergence radius of an approximation function using simple examples and verified the validity of the geometrical method. Furthermore, we verify whether each method is suitable for determining the convergence radius of the transformation matrix. An example is implemented to inspect the characteristics of the transformation matrix. The model consisted of six spring elements, as shown in Figure 3. Each spring had a stiffness of 1.3 N/m and a mass of 2 kg. The model was reduced to a master DOF with a $6-th$ DOF. The transformation matrix of the system has a size of 5×1, and Figure 4 shows the values of each component of the exact transformation matrix for frequency. In Figure 4, the component values change depending on the frequency change, in contrast to the existing methods, which have constant values even when the frequency changes. The proposed method considers these changes and uses a transformation matrix appropriate for each frequency, resulting in accurate results at high frequencies as well as low frequencies. Furthermore, Figure 4 contains as many vertical asymptotes as the number of slave DOF. Because the data are discretized, and the order of the polynomial cannot be calculated to infinity, there is a divergence interval near the singularity. Mathematically, the singularities can be found through eigenvalue analysis, and they are satisfied when λ is one of the reciprocals of the eigenvalues of $\mathbf{K}_{ss}^{-1}\mathbf{M}_{ss}$. In addition, to determine the appropriate convergence range between singular points, an eigenvalue analysis of the common ratio of the transformation matrix must be performed for all frequencies. However, this method requires enormous time resources instead of obtaining wide convergence and narrow divergence sections. In the geometric method that we propose, unlike the scalar function, the convergence boundary of the matrix function is shifted according to the index of a second-order difference, owing to the interaction of matrix operations. To address this issue, the point at which the sign first changed was used as the criterion for the convergence radius. This method can obtain a relatively wide divergence range but can satisfy the convergence range in a short time. Figure 5 compares the convergence ranges of the two methods when the proposed transformation matrix includes a $100-th$ order in $\Delta\lambda$. Figure 5a shows the shape of the transformation matrix obtained using a mathematical method. Figure 5a shows that a divergence range is formed that does not approximate the singular point well, even though the order of the polynomial is significantly increased. Figure 5b shows the convergence range of the transformation matrix obtained using the proposed method. Although it had a conservative convergence range, the transformation matrix was approximated well within the convergence section. Figure 6 shows a schematic for sequentially determining the convergence interval of the transformation matrix for the frequency. When the convergence range calculated from the first centered point is complete, the point is moved to a new point by a certain distance. If the moved point is defined within the divergence range, a new point is created at half-distance, which prevents a wide divergence. By repeating this process, convergence intervals and divergence intervals were obtained, resulting in the

total width of the convergence interval being larger than that of the divergence interval. In the divergence range, the exact transformation matrix was calculated for each frequency, as in Equation (22), and the reduced models of Equations (24)–(26) were used for analysis.

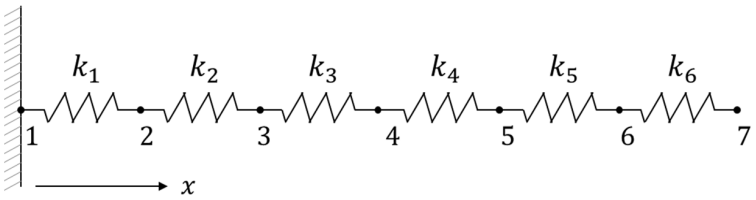


Figure 3. Discrete six degrees of freedom of the spring system.

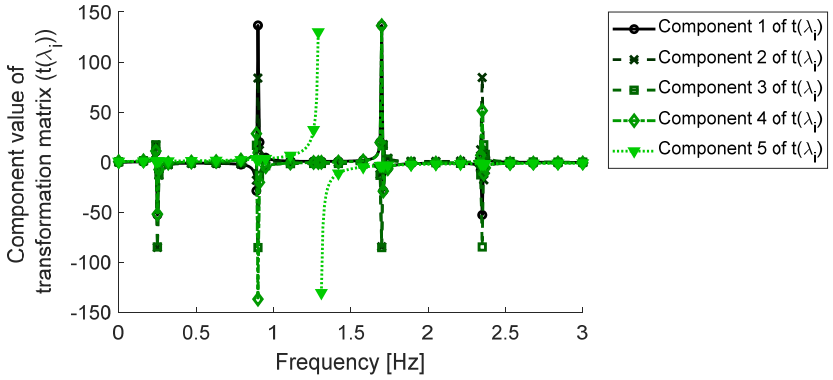


Figure 4. Component values of the exact transformation matrix of the spring model.

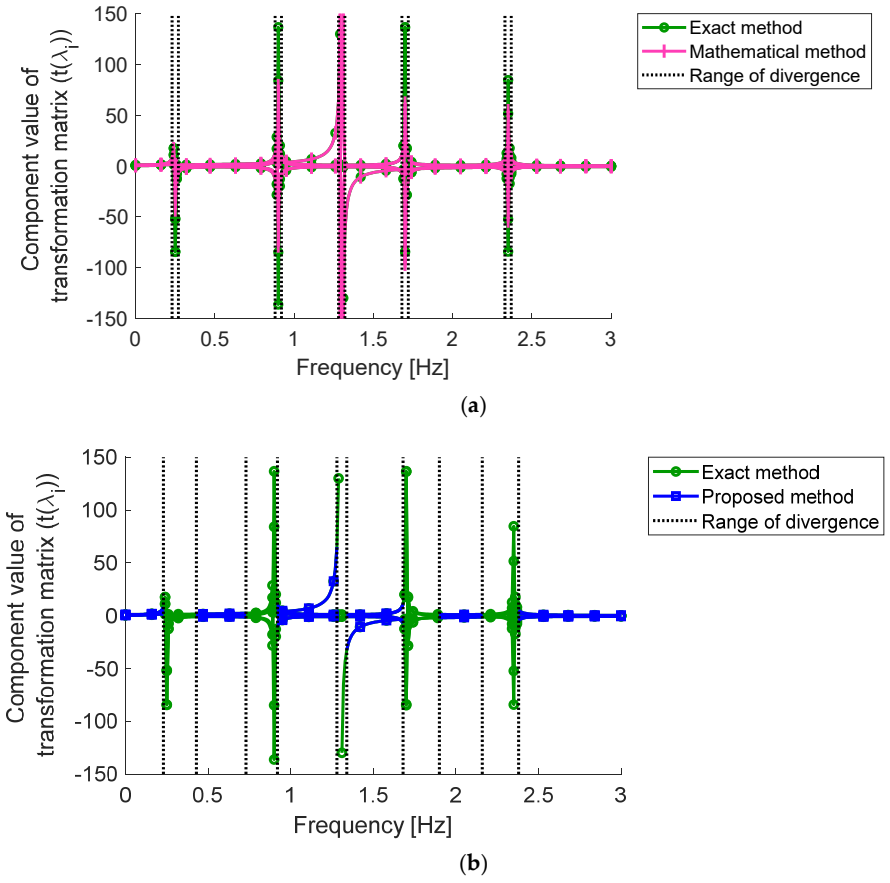


Figure 5. Comparison of convergence range and divergence range of two methods of a spring system: (**a**) Mathematical method; (**b**) Proposed method.

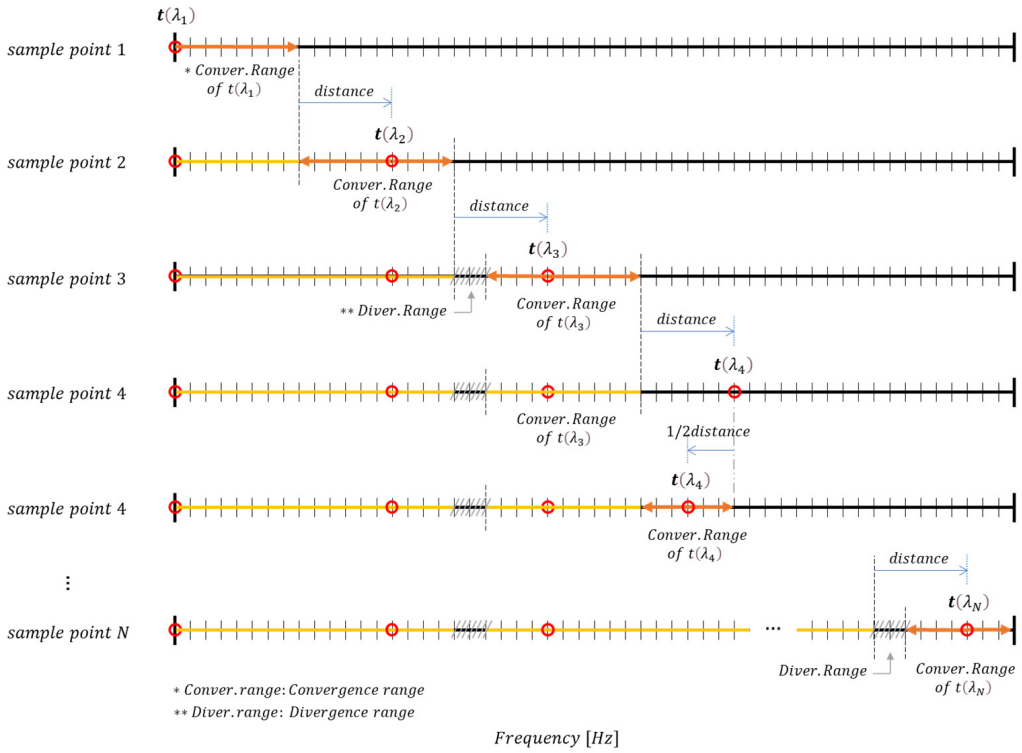


Figure 6. Schematic diagram for generating sequential adaptive transformation matrices.

3. Numerical Example

In this section, the accuracy and efficiency of the proposed method are validated using several numerical examples: i-beam, wingbox, and stage structure models. Harmonic analysis was performed to investigate the dynamic behavior of the models. All computational analyses were performed using MATLAB R2022a in a Windows 11 environment. A CPU with 64 GB memory and 14 cores running at 3.5 GHz was used for the calculations.

3.1. Example 1: I-Beam Structure Model

Figure 7 shows the finite element model of the I-beam. One side, indicated by the blue triangle, was completely fixed, and a load of -50 KN was applied in the z-direction to the midpoint of the top edge, as indicated by the black arrow in Figure 7. The exact load location is indicated by a purple x-mark. The top and bottom thicknesses of the model were 0.0088 m, and the thickness of the vertical plate was 0.0071 m. The material was assigned as structural steel, and its material properties were as follows: density of 7850 kg/m^3, elastic modulus of 200 GPa, and Poisson's ratio of 0.3. For finite element modeling, shell elements with six DOF were applied, and the total numbers of nodes and elements were 468 and 425, respectively. Out of the total 2808 DOF, approximately 0.7% or 20, were selected as master DOF. The frequency range was 0–1300 Hz, and the frequency response was confirmed for a total of 1301 frequencies at 1 Hz intervals. In this model, the transformation matrix included a $4-th$ order in $\Delta\lambda$, and the locations of the centered point, hereafter referred to as the sample point, is generated 50 Hz away from the convergence range end frequency after the initial starting position. Figure 8 presents the frequency responses of the FOM, previous ROMs, and the proposed ROM. The response of the Guyan ROM deviated from the FOM path as the frequency moved further away from 0 Hz. In the IRS response, a peak was observed at a different location from the FOM response in the high-frequency band. Ten sample points were generated within the convergence range by the proposed method, and the range accounted for approximately 82.28% of the total frequency range. The response of the proposed ROM appropriately represented the

behavior of the FOM within each convergence range. A total of 231 sample points within the divergence range were used. Figure 9 shows the calculation times for each method. The analysis of the proposed ROM was performed approximately four times faster than that of the FOM. Previous ROM showed a fast computational speed of less than 1% of the FOM computational speed. Figure 10 shows the relative error of the response of each ROM compared to the response of the FOM. The relative errors of each method for the frequency range of interest from 400 to 1300 Hz, excluding the first and second modes, were averaged as follows: Guyan ROM had a 130.66% error, IRS ROM had a 7.13% error, and the proposed ROM had a 0.23% error. The error rate of the Guyan ROM was less than 1% for frequencies below 200 Hz but then abruptly increased to more than 20%. The IRS ROM had a significant error of approximately 7% on average, but it could be difficult to express the desired behavior for ultraprecise analysis, which requires a high level of accuracy. The proposed ROM exhibited an average error rate of approximately 0.5% in the mid- to high-frequency range, verifying that it is a suitable method for such analyses.

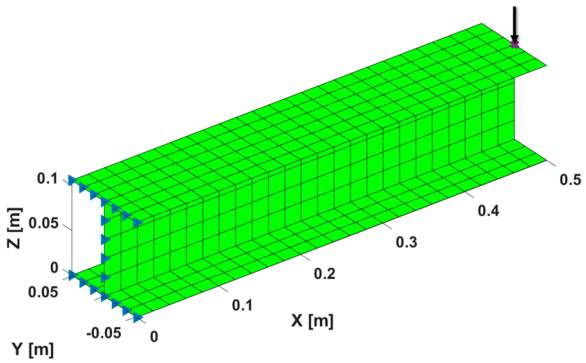


Figure 7. I−beam structure model with boundary and force conditions.

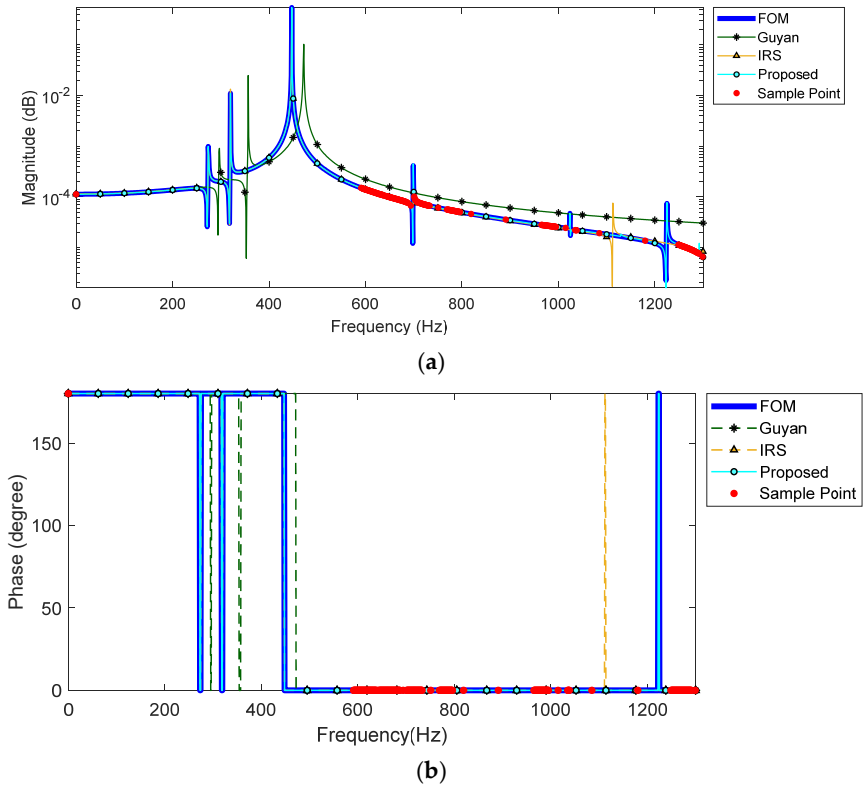


Figure 8. Comparison of frequency responses and phase angle of FOM, previous ROMs, and proposed ROM for the I−beam model: (**a**) Magnitude; (**b**) Phase angle.

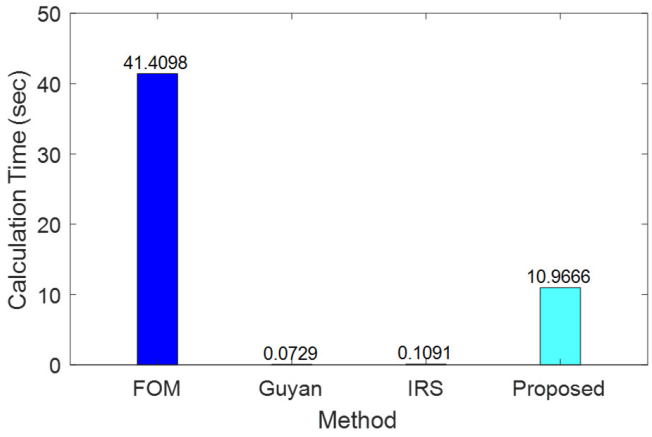


Figure 9. Comparison of calculation time of FOM, previous ROMs, and proposed ROM for the I−beam model.

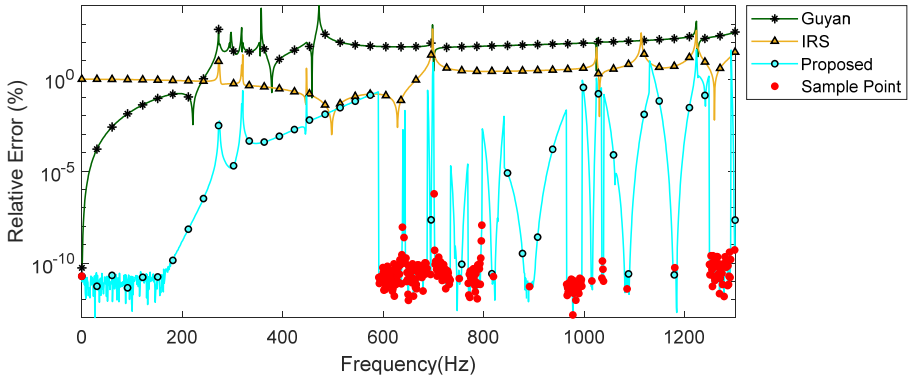


Figure 10. Comparison of relative error of previous ROMs and proposed ROM for the I−beam model.

3.2. Example 2: Wingbox Structure Model

As shown in Example 1, the existing dynamic method may be suitable for models with few elements and simple geometries. However, in the complex models, multiple similar modes are often identified within narrow frequency ranges. This leads to a complex behavioral frequency response. For this reason, existing methods in which the input frequencies are not considered in the reduced matrix are expected to show lower accuracy. Accordingly, in the following examples, additional verification is performed to inspect whether existing methods can improve accuracy when using a reduced model that additionally includes more DOF data. This requires an analysis of a finite element model with denser elements under the same analysis conditions.

Figure 11 shows a detailed view of the wingbox model consisting of 12 components: two skins, five ribs, and five spars. The thicknesses of the components were 0.023 m, 0.016 m, and 0.003 m, respectively. The model was made of an aluminum alloy with a density of 2823 kg/m^3, elastic modulus of 71 GPa, and Poisson's ratio of 0.33. The baseline model shown in Figure 12 consists of 4-node shell elements with six DOF. The number of elements was 785, the number of nodes was 676, and the total number of DOF was 4056. Additionally, the number of master DOF was 32, which was approximately 0.79% of the total DOF. The nodes with $y = 0$ at the coordinates of the model, indicated by the purple triangle, were fully constrained, and a load of -10 KN was applied to the z-axis at the end of the wingbox, as indicated by the black arrow. The exact load location is indicated by a magenta x-mark. The frequency range of this model was 0–300 Hz, and a total of 3001 frequencies were used at 0.1 Hz intervals. The transformation matrix used for the

analysis included up to the $4-th$ order in $\Delta\lambda$, and the start frequency of the next sample point was 1 Hz away from the previous section.

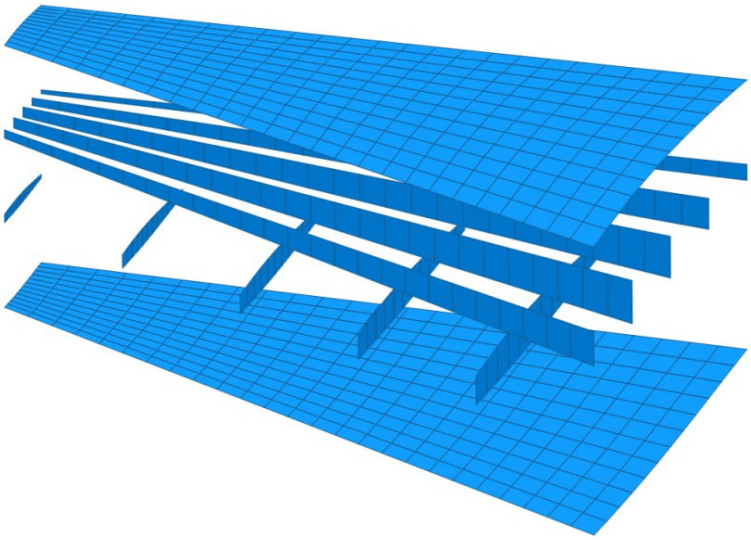


Figure 11. Wingbox structure component.

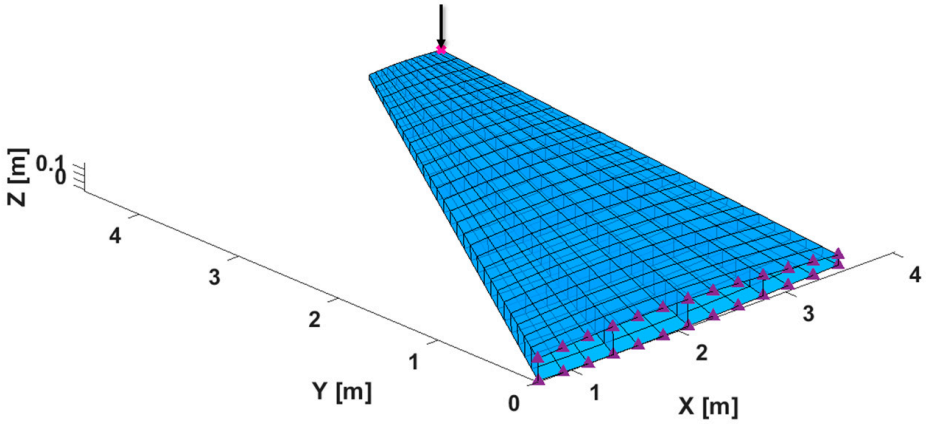


Figure 12. Baseline computational model with boundary and force conditions.

Figure 13 shows the magnitudes and phases of the frequency responses of the computational models calculated using each analysis method. The behavior of the proposed ROM was divided into two sections: convergence and divergence ranges. The convergence section accounted for approximately 99% of the total frequency, and 55 sample points were spaced in the section, unequally. The divergence range included 30 sample points. The response of the proposed ROM showed a path similar to that of the FOM. Compared to the response of the FOM, that of the Guyan ROM showed different paths after 50 Hz, whereas that of the IRS ROM showed different paths after 200 Hz. As shown in Figure 14, the proposed ROM method yields results with approximately one-quarter of the time resources of the FOM. The previous ROMs still showed a fast calculation speed of less than 1% of FOM. However, Figure 15, which shows the relative errors of each method, implies that above a certain frequency, the existing methods have such low accuracy that they cannot be used for analysis. Based on 50 Hz, where the accuracy of the Guyan method composed of low-order modes started to decrease, the frequency range was divided into a low-frequency band and a band above it, and the average error of each decreasing method was analyzed. Existing methods have errors of more than 20% in the low-frequency band and even more

than 100% in the high-frequency band. Conversely, the proposed method showed very low error rates of 2.2×10^{-4}% and 1.64% for each frequency band.

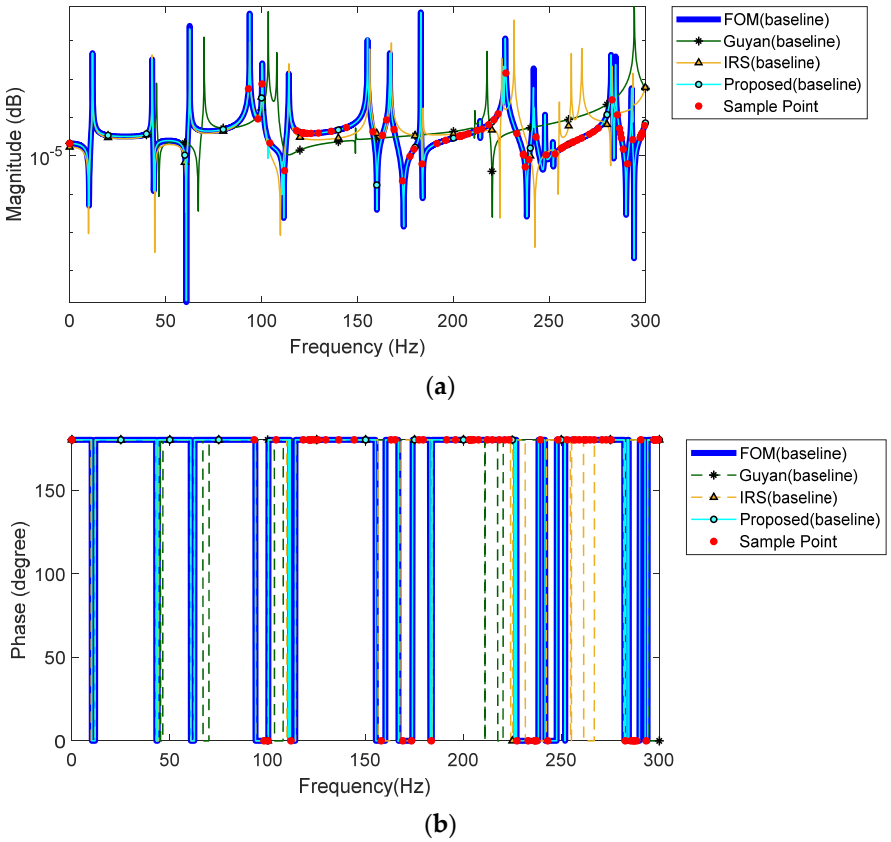


Figure 13. Frequency responses and phase angles of FOM in comparison to previous ROMs and the proposed ROM in wingbox baseline model: (**a**) Magnitude; (**b**) Phase angle.

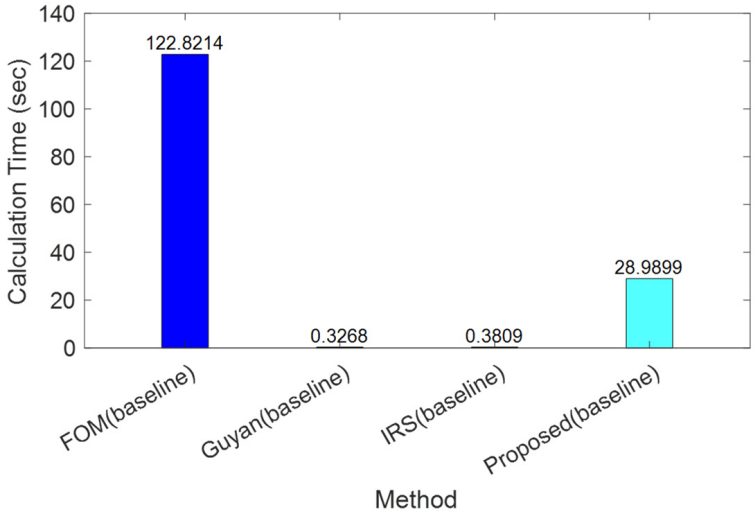


Figure 14. Comparison of calculation time of FOM, previous ROMs, and proposed ROM for the wingbox baseline model.

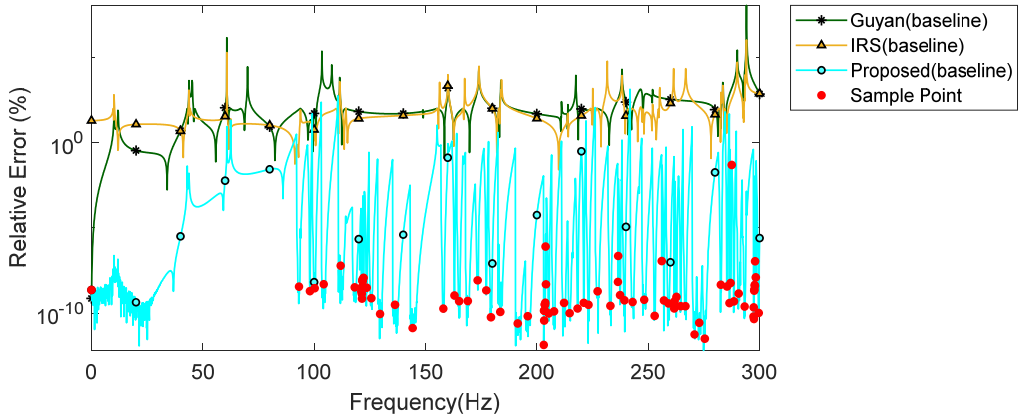


Figure 15. Comparison of relative errors of the existing ROMs and the proposed ROM for the wingbox baseline model.

In general, a reduced model with more DOF approximates the physical model better. Based on these premises, we examined whether the previous methods could improve the accuracy when constructing a ROM with an additional DOF using a dense model under the same analysis conditions. The fixed boundary conditions are indicated by the purple triangle marks, and the load locations are indicated by the magenta x marks in Figure 16. The direction and magnitude of the load are the same as those applied to the wingbox baseline model. The updated model generated by dividing the elements of the baseline model by 1/16 is shown in Figure 16. The model consisted of 12,073 nodes, 12,560 elements, and 72,438 DOF. The number of master DOF was 572, which was selected at the same ratio as in the baseline model. Figure 17 shows that the responses of the previous ROMs to the updated model are still inaccurate. Additional relative error results failed to lower the overall error line, as shown in Figure 18. The methods showed errors greater than 200% in the high-frequency band. This is because the frequency-based reduced matrix was not considered in previous ROMs. Figure 19 depicts that the existing methods invested more time in the updated model than the proposed method invested in the baseline model.

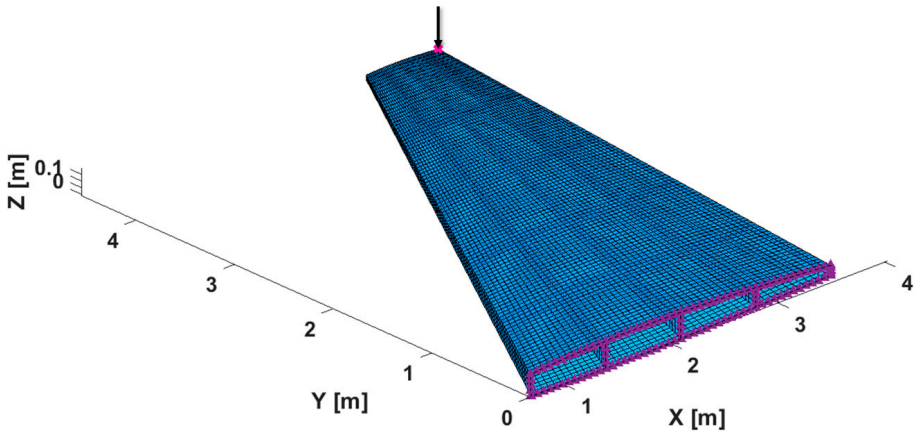


Figure 16. Fine element computational model with boundary and force conditions.

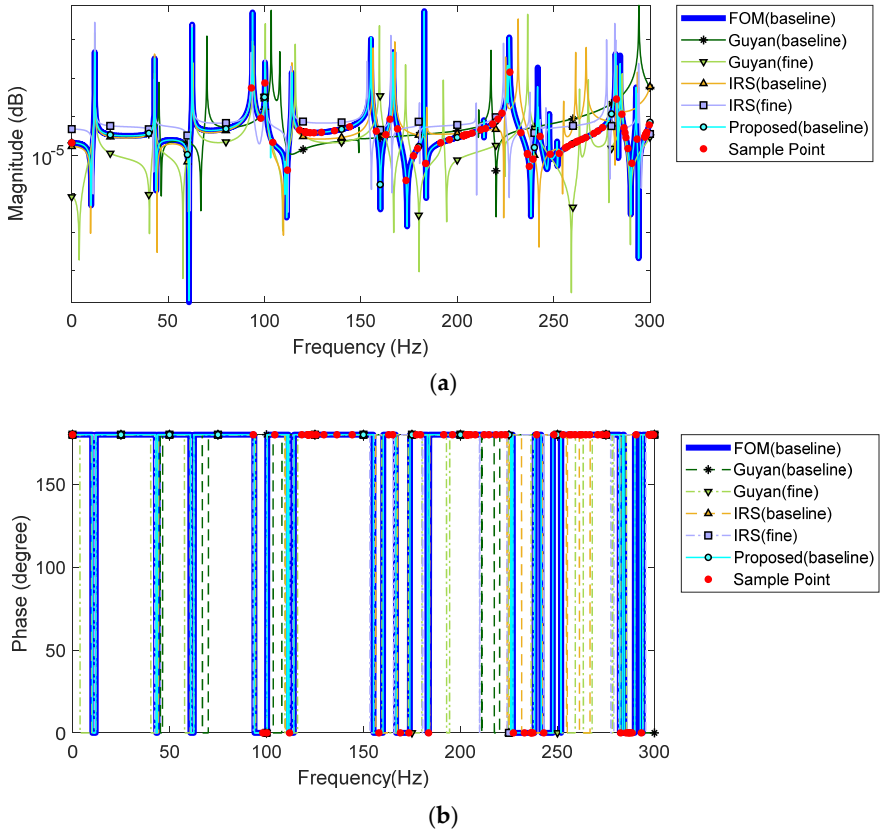


Figure 17. Additional comparison of frequency responses and phase angles using existing method for the wingbox fine model: (**a**) Magnitude; (**b**) Phase angle.

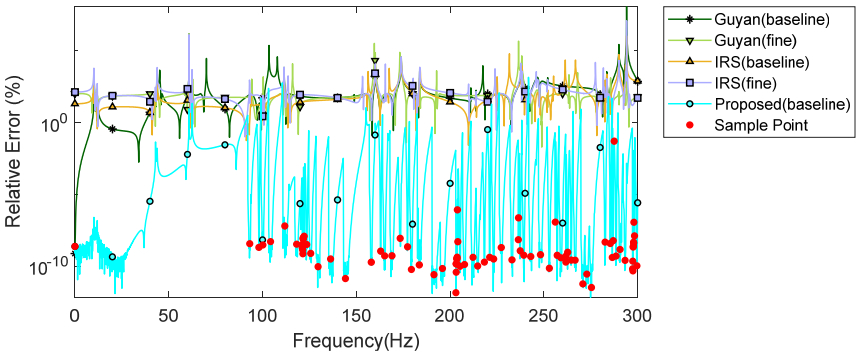


Figure 18. Additional comparison of relative errors of the existing ROMs for the wingbox fine model.

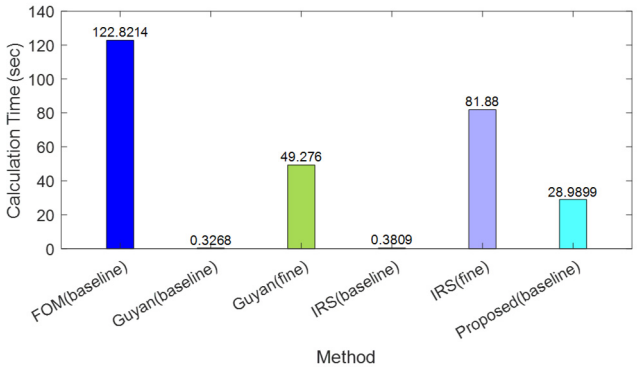


Figure 19. Additional comparison of calculation time with the existing method for the wingbox fine model.

3.3. Example 3: Stage Structure Model

Despite existing methods using ROM with additional DOF, they did not lead to any improvement in efficiency compared with the proposed method. Building on the previous findings, we intend to determine the applicability of each ROM method to a larger model. The numerical model was analyzed using the steps described in Section 3.2.

The final example is the ultra-precision stage model. The model consisted of structural steel, aluminum alloys, and a metal–matrix composite. The alloy was 6061-T6 with a Young's modulus of 69 GPa, density of 2703 kg/m^3 and Poisson's ratio of 0.33. The composite had a Young's modulus of 110 GPa, density of 2870 kg/m^3 and Poisson's ratio of 0.2. Figure 20 depicts the simulation model of the numerical example. The models consisted of solid elements with three DOF per node, 15,707 elements, 19,139 nodes, and 57,417 DOF. One hundred master DOF were randomly selected, representing approximately 0.17% of the total DOF. The bottoms of the six legs, indicated by the magenta triangle, were fully fixed, and a load of 500 KN was applied to the yellow circle in the y-direction, as indicated by the black arrow. The frequency range was 0–800 Hz, and the analysis was performed for a total of 8001 frequencies at 0.1 Hz intervals. Consecutive sample points were spaced 10 Hz apart from the previous section. The transformation matrix used for the analysis included terms up to the $7-th$ order in $\Delta\lambda$.

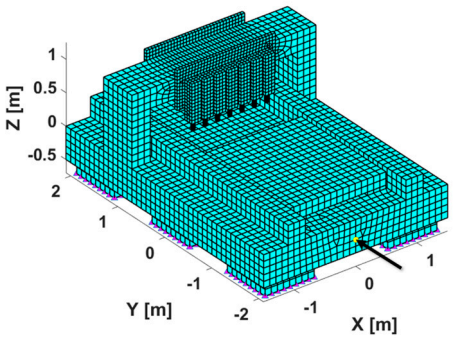


Figure 20. A baseline simulation model of ultra-precision stage with boundary and force conditions.

Figure 21 shows the frequency response of the simulation model computed using the four analytical methods. Using the proposed method, 25 sample points were adopted within the convergence range, and 791 individual reduced models were generated within the divergence range. The convergence range accounted for approximately 90% of the total frequency. The response of the proposed ROM followed that of the FOM, in contrast to other ROMs that diverged from the FOM results. The phase angles in Figure 21b depict that the results of the previous ROMs were out-of-phase even at the first peak. Figure 22 shows the relative errors for each reduced method. As shown in Figure 22, the relative error of the proposed ROM is significantly lower than that of the previous ROMs. When the frequency of interest was narrowed down to 300 to 800 Hz, excluding low modes, and the average relative error of each method was compared, the proposed ROM had an insignificant error of 1.06%. However, the previous ROMs showed excessive error rates of over 25% for Guyan and over 80% for IRS. Figure 23 compares the computation times of all simulation models. In Figure 23, while FOM analysis required 7860 s, the proposed method performed an accurate analysis in 4333.4 s, where its efficiency was approximately 181.4% compared to FOM analysis. The previous ROMs required minimal computation time but had low accuracy, as shown in Figure 22.

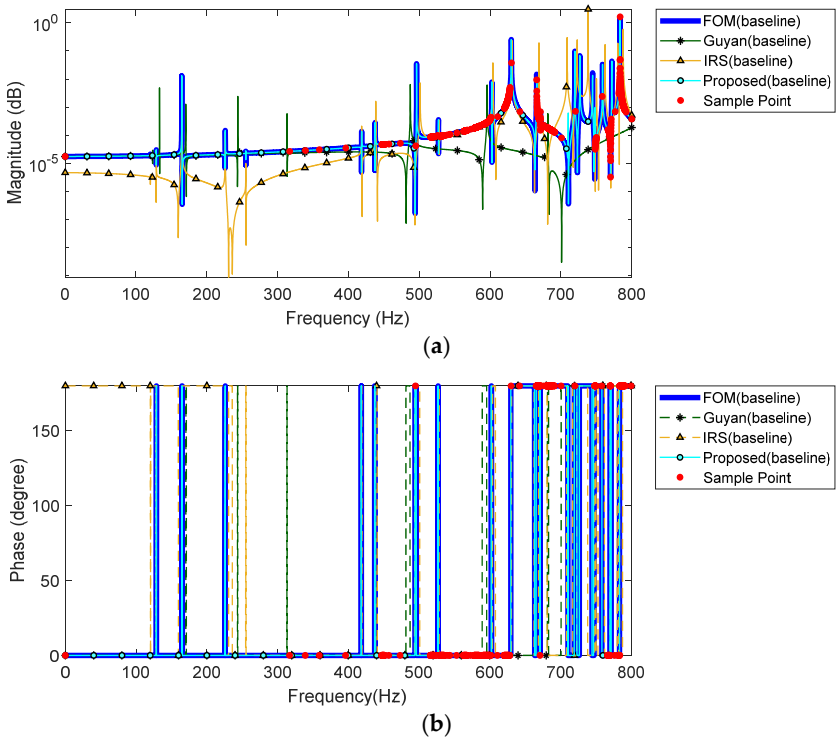


Figure 21. Frequency responses and phase angles of FOM in comparison to previous ROMs and proposed ROM for the wingbox baseline model: (**a**) Magnitude; (**b**) Phase angle.

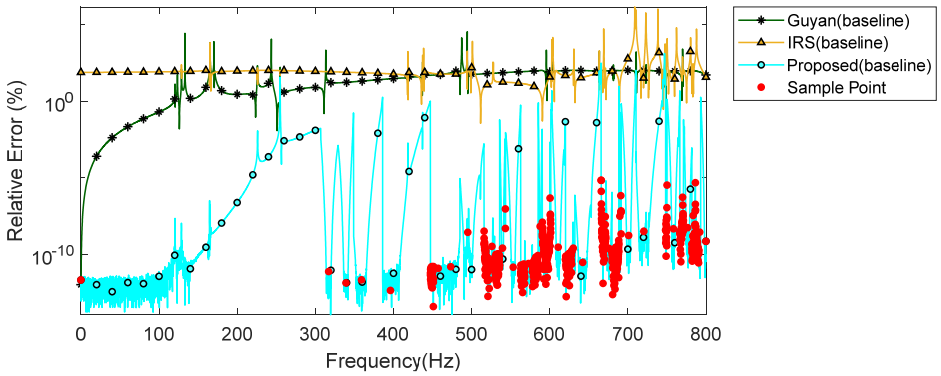


Figure 22. Comparison of relative errors of previous ROMs and proposed ROM for the stage baseline model.

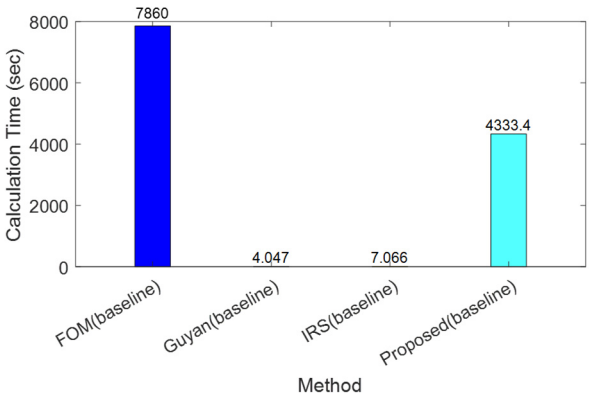


Figure 23. Comparison of calculation time of FOM, previous ROMs, and proposed ROM for the stage baseline model.

An additional analysis was performed on the updated model to determine whether the accuracy of the existing method could be improved with additional DOF. The updated model is shown in Figure 24. The fine model had elements a quarter the size of the baseline model, with 125,656 elements, 140,683 nodes, and 422,049 DOF. The number of master DOF was selected at a higher rate than the baseline model with 2210 selected, which was approximately 0.5% of the total DOF. The boundary conditions are still applied to the bottoms of the legs, indicated by the purple triangles, and the load condition and location are the same as in the stage baseline model. In Figure 25a, it is confirmed that the response of the previous ROMs for the fine model is not similar to the behavior of the FOM. In Figure 26, the additional results of the existing method for the narrowed frequency range show that accuracy did not improve, presenting an error of more than 200%. Figure 27 shows that the existing methods invested sufficient time to improve accuracy.

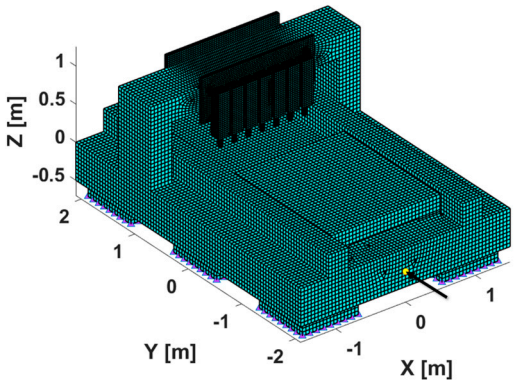


Figure 24. Fine element simulation model with boundary and force conditions.

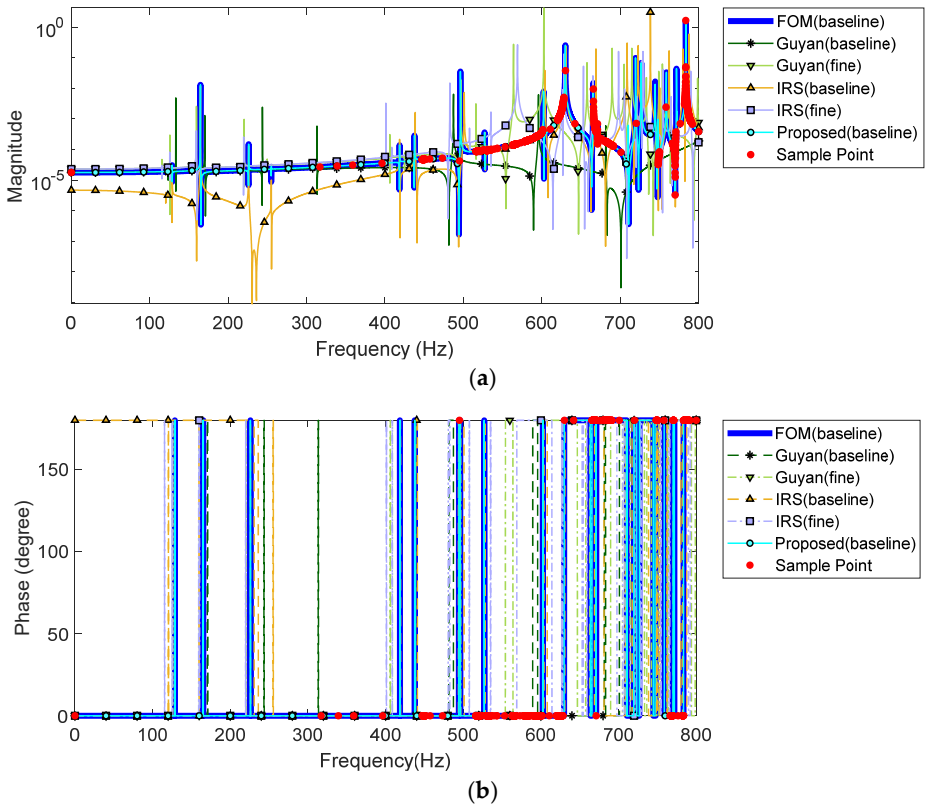


Figure 25. Additional comparison of frequency responses and phase angles using existing method for the stage fine model: (**a**) Magnitude; (**b**) Phase angle.

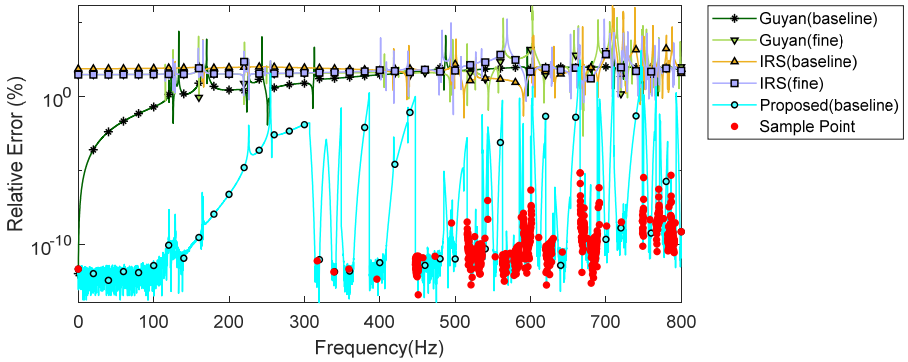


Figure 26. Additional comparison of relative errors of existing ROMs for the stage fine model.

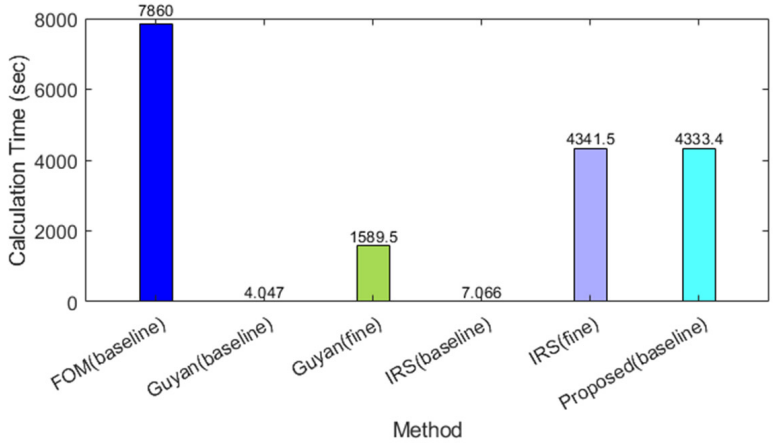


Figure 27. Additional comparison of calculation time with the existing method for the stage fine model.

4. Conclusions

In this paper, an accurate frequency-based reduction method for broadband frequency analysis using the Taylor series was proposed. As a new reduced model was generated at all frequencies, accuracy was ensured even in the high-frequency range. The frequency range was divided into convergence and divergence sections using a geometrical convergence test of the transformation matrix. The transformation matrix generated in the convergence section is reused by updating the interval for each frequency, which provides efficiency. In the divergence section, a frequency-dependent reduced model was generated for each frequency to provide accuracy. Three numerical examples are considered to demonstrate the performance of the proposed method. Existing reduction methods consisting of a single reduction matrix have limitations in terms of accuracy. The proposed method presented convergence sections of over 80% for all examples and achieved high accuracy with an error rate of less than 2% in the frequency range of interest. In addition, compared with the respective computation times of FOM, the proposed method demonstrated a maximum efficiency of approximately 23.6% and a minimum efficiency of approximately 55.1% of FOM analysis time. However, the proposed method has a limitation in that its computational efficiency decreases as the divergence range widens because it performs a new matrix operation every time in the divergence range. Thus, the reduction method in the divergence section needs to be improved in terms of computation time through additional research. For example, the damping effect is expected to reduce the singularity value and improve the divergence range.

This proposed method can be extended to independently separate the physical parameters of the system, as well as the frequency, in the future. This separation allows for

rapid calculation of the changed parts by immediately reflecting the changes in the material properties. Additionally, this method can be applied to systems whose properties change depending on the frequency, such as rubber mounts in vehicles.

Author Contributions: Conceptualization, J.L.; methodology, G.C. and J.L.; software, G.C. and S.C.; validation, G.C. and S.C.; formal analysis, G.C. and S.C.; investigation, G.C., J.L. and S.C.; resources, G.C. and J.L.; data curation, G.C. and S.C.; writing—original draft preparation, G.C; writing—review and editing, J.L. and S.C.; visualization, G.C. and S.C.; supervision J.L. and S.C.; project administration, S.C.; funding acquisition, S.C. All authors have read and agreed to the published version of the manuscript.

Funding: This work was supported by the Innovative Small Modular Reactor Development Agency grant funded by the Korea Government (MOTIE) (No. RS-2024-00405419).

Data Availability Statement: Data are contained within the article.

Conflicts of Interest: The authors declare no conflicts of interest.

References

1. Hua, X.; Thomas, A.; Shultis, K. Recent progress in battery electric vehicle noise, vibration, and harshness. *Sci. Prog.* **2021**, *104*, 00368504211005224. [CrossRef]
2. Karunakaran, V.; Kandadai Nagaratnam, S. Electromagnetic, vibration and thermal analysis of 1.1 kw switched reluctance motor for electric vehicle application. *J. Electr. Eng. Technol.* **2023**, *18*, 1809–1820. [CrossRef]
3. Hazra, S.; Reddy, K.J. Development of powertrain mounting system for high frequency characteristics optimisation in electric vehicles. *Int. J. Electr. Hybrid Veh.* **2023**, *15*, 234–255. [CrossRef]
4. Zhao, M.; Wang, X.; Liu, L.; Tu, X.; Yang, Q. Optimization of PMSM for EV based on vibration and noise suppression. *Appl. Comput. Electromagn. Soc. J.* **2024**, *39*, 64–80. [CrossRef]
5. Przemieniecki, J.S. Matrix Structural Analysis of Substructures. *AIAA J.* **1963**, *1*, 138–147. [CrossRef]
6. Hurty, W.C. Dynamic analysis of structural systems using component modes. *AIAA J.* **1965**, *3*, 678–685. [CrossRef]
7. Craig, R.; Bampton, M.C. Coupling of substructures for dynamic analysis. *AIAA J.* **1968**, *6*, 1313–1319. [CrossRef]
8. Lucia, D.J.; Beran, P.S.; Silva, W.A. Reduced-order modeling: New approaches for computational physics. *Prog. Aerosp.* **2004**, *40*, 51–117. [CrossRef]
9. Sung, H.; Chang, S.; Cho, M. Structural system identification via a reduced system and sensor-location selection method. *AIAA J.* **2019**, *57*, 2109–2122. [CrossRef]
10. Kim, J.G.; Seo, J.; Lim, J.H. Novel modal methods for transient analysis with a reduced order model based on enhanced Craig–Bampton formulation. *Appl. Math. Comput.* **2019**, *344*, 30–45. [CrossRef]
11. Ahn, J.G.; Yang, H.I.; Kim, J.G. Multipoint constraints with Lagrange multiplier for system dynamics and its reduced-order modeling. *AIAA J.* **2020**, *58*, 385–401. [CrossRef]
12. Oh, S.; Ahn, C.U.; Ahn, K.; Kim, J.G. Implicit inverse force identification method for vibroacoustic finite element model. *J. Sound Vib.* **2023**, *556*, 117713. [CrossRef]
13. Guyan, R.J. Reduction of stiffness and mass matrices. *AIAA J.* **1965**, *3*, 380. [CrossRef]
14. O'Callaghan, J. A procedure for an improved reduced system (IRS) Model. In Proceedings of the 7th International Modal Analysis Conference, Las Vegas, NV, USA, 30 January–2 February 1989; pp. 17–21.
15. Friswell, M.I.; Garvey, S.D.; Penny, J.E.T. Model reduction using dynamic and iterated IRS techniques. *J. Sound Vib.* **1995**, *186*, 311–323. [CrossRef]
16. Xia, Y.; Lin, R.N. Improvement on the iterated IRS method for structural eigensolutions. *J. Sound Vib.* **2004**, *270*, 713–727. [CrossRef]
17. Weng, S.; Tian, W.; Zhu, H.; Xia, Y.; Gao, F.; Zhang, Y.; Li, J. Dynamic condensation approach to calculation of structural responses and response sensitivities. *Mech. Syst. Signal Process.* **2017**, *88*, 302–317. [CrossRef]
18. Jeong, J.; Baek, S.; Cho, M. Dynamic condensation in a damped system through rational selection of primary degrees of freedom. *J. Sound Vib.* **2012**, *331*, 1655–1668. [CrossRef]
19. Chang, S.; Cho, M. Dynamic-condensation-based reanalysis by using the Sherman–Morrison–Woodbury formula. *AIAA J.* **2021**, *59*, 905–911. [CrossRef]
20. Yang, C.; Xia, Y. Optimal sensor placement based on dynamic condensation using multi-objective optimization algorithm. *Struct. Multidiscip. Optim.* **2022**, *65*, 210. [CrossRef]

21. Lee, J.; Park, Y.; Lee, Y.; Chang, S. An adaptive frequency sampling algorithm for dynamic condensation-based frequency response analysis. *Mathematics* **2023**, *11*, 2683. [CrossRef]
22. Newmark, N.M. A method of computation for structural dynamics. *J. Eng. Mech. Div.* **1959**, *85*, 67–94. [CrossRef]

Disclaimer/Publisher's Note: The statements, opinions and data contained in all publications are solely those of the individual author(s) and contributor(s) and not of MDPI and/or the editor(s). MDPI and/or the editor(s) disclaim responsibility for any injury to people or property resulting from any ideas, methods, instructions or products referred to in the content.